Int. J. Heat Mass Transfer. Vol. 32, No. 6, pp. 1063–1076, 1989
Printed in Great Britain

0017–9310/89 $3.00 + 0.00

Melting in an enclosure heated at constant rate

ZONGQIN ZHANG and ADRIAN BEJAN
Department of Mechanical Engineering and Materials Science, Duke University, Durham, NC 27706, U.S.A.

(*Received* 26 *May* 1988 *and in final form* 5 *September* 1988)

Abstract—This paper describes a two-part study of the time-dependent melting of an enclosed phase-change material heated at a constant rate from the side. The first part describes experimental measurements with n-octadecane conducted in a 74 cm tall enclosure. The heat flux Rayleigh numbers of these experiments are of the order of 10^{13}, and the liquid flow pattern is weakly turbulent. The second part of the study describes the liquid-superheat effect analytically, by means of a 'matched boundary layers' solution for the convection regime of the heat transfer and melting process. The predicted overall Nusselt number relationship agrees very well with the empirical correlation based on experiments.

1. INTRODUCTION

THIS PAPER describes a two-part study of the process of melting in the presence of natural convection in an enclosure that is being heated at a constant rate. The general subject of natural convection melting in enclosures has received considerable attention, because of its applicability in areas such as thermal energy storage, metallurgy, manufacturing and geophysics. The existing work, however, is primarily based on the model in which the heating effect is provided by an isothermal side wall the temperature of which remains fixed in time (see, e.g. the two reviews by Viskanta [1, 2]). The constant-rate heating mode deserves to be studied because it can serve as a good model for the operation of latent-heat storage devices for solar energy.

The first part of the paper (Section 2) describes a series of laboratory experiments conducted in a considerably taller enclosure than in the existing experimental studies, that is, at high Rayleigh numbers where the flow shows signs of turbulence. The second part of the study consists of a compact boundary layer analysis of the convection-dominated regime.

Therefore, in addition to the new focus on the constant-rate heating mode, two additional objectives of this study are to extend the high Rayleigh number domain experimentally (Section 2), and to document analytically the effect of liquid superheat in the convection regime (Section 3).

2. EXPERIMENTAL STUDY

2.1. *Apparatus*

The vertical enclosure in which the experiments were performed is shown in Fig. 1. The enclosure was filled with the paraffin n-octadecane, the purity of which was 99%. The melting point reported by the manufacturer (Eastman Kodak) is 28°C. This phase-change material was preferred because it has been used in many of the existing experimental studies, and because it has a well-defined melting point near room temperature. A compilation of the thermophysical properties of this material can be found in a paper by Bennon and Incropera [3].

The enclosure is defined by two parallel vertical plates positioned 14.6 cm apart. The top, bottom and side walls are made out of acrylic plexiglas 2.5 cm thick. This material permits the viewing of the flow and the solid–liquid interface; at the same time it provides good structural strength and thermal insulation characteristics over a wide range of temperatures. The height of the enclosed space is 73.7 cm. The length, or what would be the dimension in the direction normal to the plane of Fig. 1, is 56 cm: this dimension is large enough to minimize the three-dimensional (end) effects on the flow and the two-phase interface. While seeking to eliminate these effects, one must compare the 56 cm dimension with the average thickness of the liquid region (2–4 cm) and with the vertical boundary layer thickness (~ 5 mm), not with the 14.6 cm thickness of the enclosed space, which is occupied mostly by solid.

The aluminium hot plate has a thickness of 1.8 cm. It is heated by eight uniformly spaced strip heaters attached horizontally to the outer side of the plate. The total heat transfer rate is determined by measuring the electrical power dissipated in the strip heaters.

The temperature of the opposite aluminum plate is regulated by circulating a stream of alcohol through a hollow space machined into that plate. The stream can be heated or cooled by flowing through a constant-temperature bath refrigerator, which is capable of controlling the alcohol temperature to within ± 0.1°C.

The enclosure is supported by a wooden frame and surrounded by a 15 cm thick layer of fiberglass insulation housed in an outer plywood container. This insulating cover was originally built for an experiment on natural convection in a triangular enclosure [4], in which the heated plate of the present apparatus served

NOMENCLATURE

c	specific heat of liquid
c_s	specific heat of solid
C	constant of integration, equation (25)
F	function, $\hat{\delta}^3\hat{T}_c$
g	gravitational acceleration
h_{sf}	latent heat of fusion
H	height of liquid region
k	thermal conductivity of liquid
Nu	Nusselt number, equation (7)
q''	heat flux through the heated wall
Ra_*	Rayleigh number based on heat flux and height H, equation (5)
$Ra_{\Delta T}$	Rayleigh number based on average temperature difference, defined under equation (30)
s	local thickness of the liquid region
s_{av}	height-averaged thickness of the liquid region, equation (2)
Ste	Stefan number based on the overall temperature difference scale in the convection regime, equation (15)
Ste_*	Stefan number based on heating rate, equation (4)
Ste_s	solid subcooling Stefan number, equation (6)
t	time
t_0	start-up time
T	excess temperature above the melting point in Section 3
T_{avg}	height-averaged temperature of the heated wall, equation (1)
T_c	liquid core temperature
T_m	melting point of phase-change material
T_s	temperature of the solid phase, equation (6)
T_w	temperature of the heated wall
$\hat{T}_w$	dimensionless wall temperature, $(T_w k/q''H)Ra_*^{1/5}$
ΔT	temperature difference, $T_w - T_m$
u, v	velocity components, Fig. 9
u_0	local melting rate, equation (12)
$(u_r)_{-\lambda}$	entrainment velocity of the warm boundary layer
u_δ	entrainment velocity of the cold boundary layer
V	vertical velocity coefficient, equation (11)
x, y	coordinate system attached to the two-phase interface, Fig. 9
x_r, y	coordinate system attached to the heated wall, Fig. 9
$\hat{y}$	dimensionless vertical position, y/H.

Greek symbols

α	thermal diffusivity of the liquid
β	volume expansivity of the liquid
δ	thickness of the cold thermal boundary layer
$\hat{\delta}$	dimensionless cold boundary layer thickness, $(\delta/H)Ra_*^{1/5}$
θ_*	dimensionless time, $tq''/\rho h_{sf}H$
$\theta_*^{(0)}$	dimensionless time based on $(t-t_0)$, equation (3)
λ	thickness of the warm thermal boundary layer
$\hat{\lambda}$	dimensionless warm boundary layer thickness, $(\lambda/H)Ra_*^{1/5}$
ν	kinematic viscosity of the liquid
ρ	density of the phase-change material, liquid or solid.

as the base plate for the triangular enclosure. Measurements showed that the heat leak from the heated enclosure to the ambient does not exceed 1.5% of the total heat input to the heated plate.

2.2. *Measurements*

The temperature distributions along the two differentially heated vertical walls were measured by means of thermocouples positioned at four different altitudes in the vertical mid-plane of the apparatus. The thermocouple positions are indicated in Fig. 1: measured from the bottom of the enclosure, the altitudes of the thermocouples are 17.5, 27, 56 and 66 cm. Each thermocouple was made out of chromel–alumel (type K) wire and embedded from the outside, to within 1.6 mm of the inside surface of each plate. The temperature readings provided by them were accurate to within ± 0.2°C.

The heat flux on the dry side of the heated wall was not measured directly, however, the eight strip heaters were spaced and powered uniformly, in order to ensure a uniform distribution of the heating effect. The unheated gaps between the strip heaters were smoothed over by the longitudinal conduction through the aluminum plate: this secondary effect is discussed further in Section 4. The heat flux q'' was calculated by dividing the known heater power input by the total area of the heated plate.

The temperature distribution through the liquid and solid phases of the phase-change material was measured with four thermocouple rakes containing 55 thermocouples arranged on four levels (Fig. 1). The distances between each rake and the bottom of the enclosure are 12, 28.5, 45 and 61.5 cm. On each rake, the thermocouples were positioned closer together in the vicinity of the heated wall, i.e. in the region occupied by liquid. The temperature readings were recorded with an auto-print digital voltmeter,

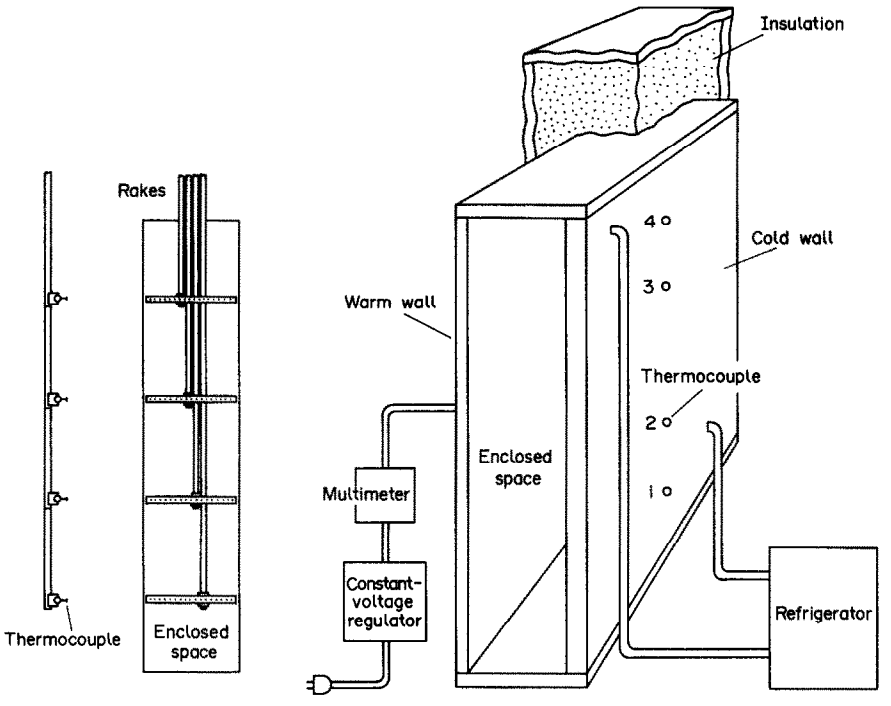

FIG. 1. Scale drawing showing the experimental apparatus and instrumentation.

the dwell time per thermocouple of which is 3 s. This time interval is short when compared with the duration of one heating and melting run (Figs. 5 and 6).

The instantaneous shape of the liquid–solid interface was photographed by looking parallel to the interface, through the transparent side walls. The usual time interval between two consecutive photographs was 30 min. The instantaneous shape of the interface was measured from a blow-up of the photograph, and recorded in terms of (s, y) pairs of numerical values describing the horizontal thickness of the liquid region and the corresponding altitude.

The instantaneous volume of the liquid region was calculated numerically by integrating the area under the $s(y)$ curve described in the preceding paragraph. The integration was based on Simpson's rule. The accuracy of this liquid volume (or melt fraction) calculation was evaluated for each run by comparing the calculated value with the actual quantity of liquid accumulated at the end of the run. The physical measurement of the end-of-run liquid volume consisted of rapidly draining the liquid into a clean container, and then weighing the contents. In all the melting experiments described in this paper, the difference between the liquid amount calculated from photographs and the amount measured directly was less than 1.5%.

The most critical phase of each run was the filling of the enclosure with liquid paraffin. In order to avoid the formation and trapping of air bubbles, only a small amount of paraffin was poured into the enclosure (one 1 cm deep layer at a time) and solidified before the addition of the next layer. The 1 cm deep layers are visible as striations (horizontal, equidistant shadows) in the solid situated in the vicinity of the liquid space in Fig. 2. An air space with a depth of 3 cm was left at the top of the enclosure in order to accommodate the expansion of the paraffin during melting. The liquid expansion effect was counteracted by intermittently drawing enough liquid so that the level of the liquid pool did not rise during the experimental run. Because of the large height of the apparatus, the filling and solidification phase that preceded each run lasted approximately one week.

Before the start of one experiment, the fully solidified paraffin was brought to a state of uniform temperature by circulating constant-temperature alcohol through the jacket of one of the vertical plates. This phase lasted approximately 48 h. Finally, the heating run started by simultaneously discontinuing the alcohol circulation and powering the resistance heaters attached to the other vertical plate. The power dissipated by the heater was constant during the entire duration of the experiment.

2.3. *Results*

Figure 2 shows a sequence of photographs of the liquid–solid interface. For better viewing, positioned to the right of each photograph is a line drawing of the two-phase interface. The shape of the region occupied by the liquid phase has the same general features as the liquid regions photographed in melting experiments near a constant-temperature wall (e.g. Hale and Viskanta [5]). The upper end of the liquid

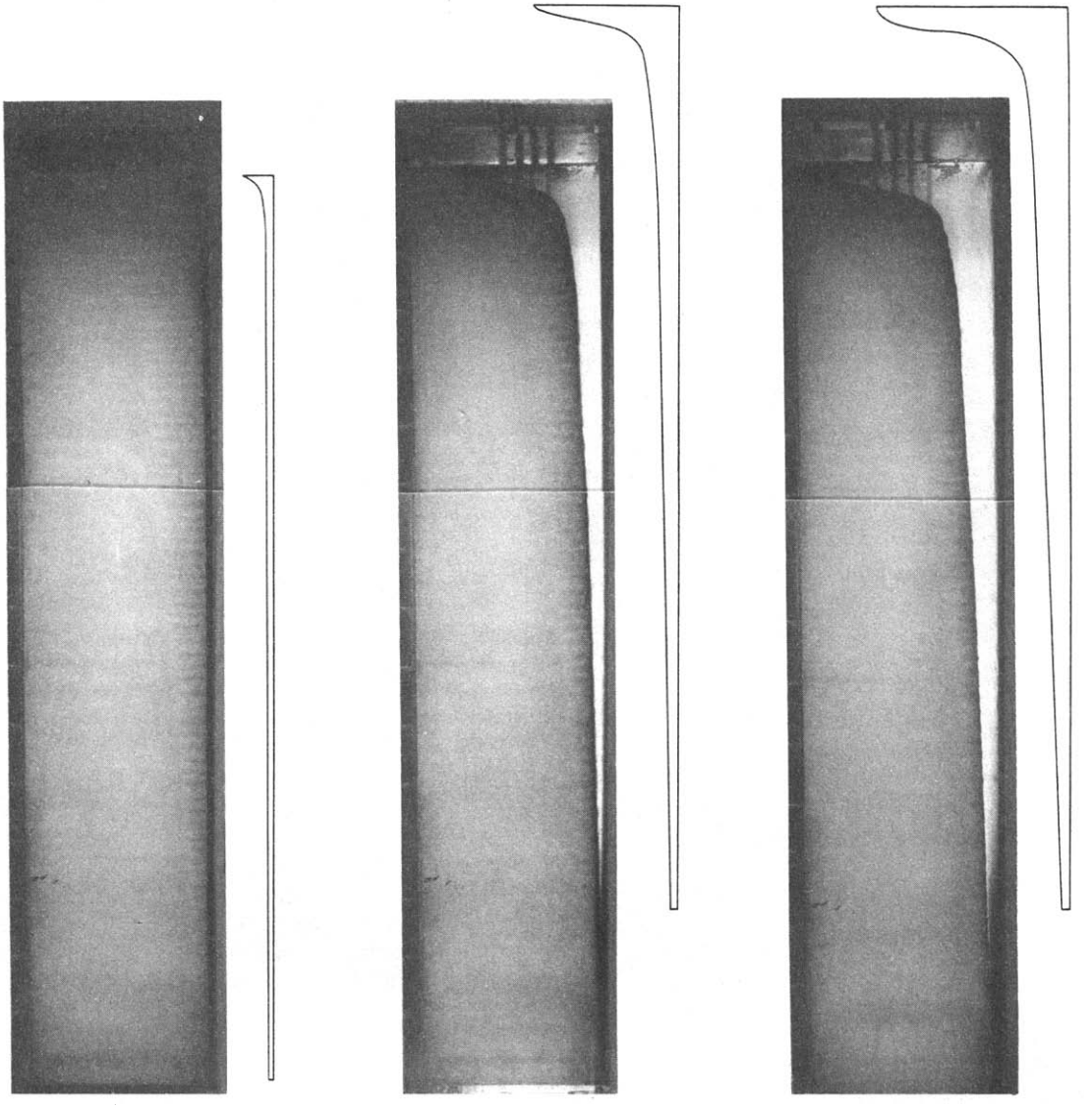

FIG. 2. Sequence of photographs showing the evolution of the two-phase interface in the late convection-dominated stages of an experiment when $Ra_* = 2.34 \times 10^{13}$ (from left to right, $\theta_* = 0.01$, 0.025, 0.0345, where θ_* is defined in the Nomenclature).

region expands horizontally faster than the rest of the region, as the vertical warm jet created by the heated plate makes a 90° turn and impinges directly on the upper end of the liquid–solid interface.

The three photographs of Fig. 2 correspond to relatively 'late' stages of the convection regime. The scale analysis of the melting process shows that the transition from the conduction-dominated regime to the convection regime occurs at a time θ_* of the order of $Ra_*^{-1/5}$, where $\theta_* = tq''/\rho h_{sf} H$ and Ra_* is defined in equation (5). The same time scale is associated with the wall temperature maximum and Nu minimum visible in Figs. 5 and 8. Since in the photographs of Fig. 2 $Ra^* = (2.34)10^{13}$, the transition to the convection regime occurs when $\theta_* \sim Ra_*^{-1/5} \sim 0.002$. This dimensionless time is one order of magnitude shorter than the time when the first of the photographs was taken. This observation and the first photograph of Fig. 2 suggest that the shape of the two-phase interface is nearly plane during the earlier stages of the convection regime. Photographs of these earlier stages were taken, however, they have not been added to Fig. 2 because for the frontal area occupied by liquid they show nothing more than a narrow dark strip of nearly constant thickness.

The shape of the liquid–solid interface was two-dimensional over most of the 56 cm width measured in the direction normal to Fig. 1. This high degree of two-dimensionality is due to the large size, adequate insulation and symmetry that were built into the apparatus and the distribution of side heating. Deviations from the two-dimensional shape occurred only

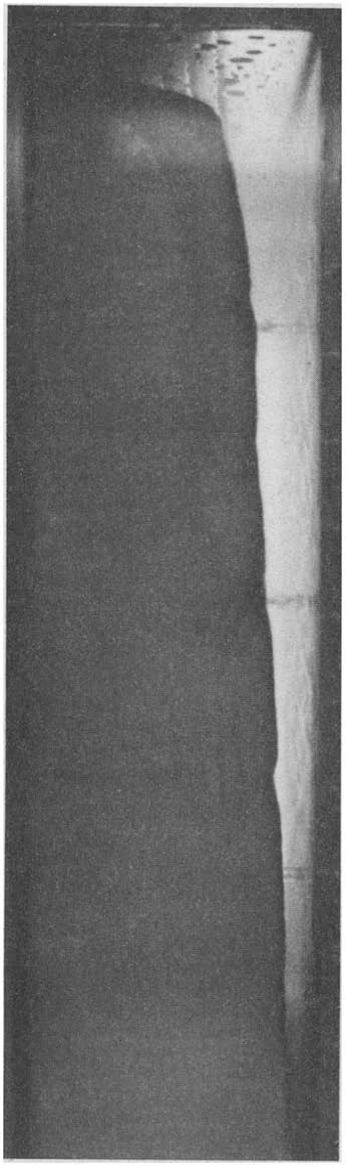

FIG. 3. View of the inside surface of the heated plate during a late convection stage, showing the presence of turbulence in the vertical boundary layer flow near the heated plate ($Ra_* = 4.9 \times 10^{12}$, $\theta_* = 0.039$).

along the edges of the interface, that is, along the lines of contact with the lateral plexiglas windows. These deviations (irregularities in shape, actually) were caused by the few air bubbles that remained trapped on the windows during the filling and solidification phase. The view presented in Fig. 3 shows these irregularities: this particular photograph was taken from an angle, that is, by looking at the surface of the heated plate.

Figure 3 shows further that the boundary layer flow near the heated plate is turbulent. Similar observations were made while looking at the flow descending along the two-phase interface. The presence of turbulence is due to the high Rayleigh number domain covered by this study.

The history of the temperature distribution along the heated plate is illustrated in Fig. 4. There are three important features to note in this figure. First, there is a relatively short time interval ('start-up' time, t_0), during which the temperature of the heated plate rises from the ambient level to the melting point of the phase-change material. The start-up time t_0 was of the order of 15 min, as is described in the paragraph that precedes equation (3).

Immediately following the start-up time interval is a period when the temperature of the plate is uniform and rises linearly in time. This second period corresponds to the melting regime that is ruled by pure conduction. Finally, Fig. 4 shows how the wall temperature reaches a plateau in the convection melting regime. In this final phase, the boundary layer convection and thermal stratification of the liquid region sustain a vertical temperature gradient along the heated plate. The temperature distribution along the heated plate is similar to the distribution found along the vertical walls of a rectangular cavity with pure natural convection (i.e. no melting) and heated and cooled with uniform heat flux from the side [6].

The temperature of the heated wall reaches a weak maximum before settling for the long-time level dictated by convection. The temperature maximum and its position in time are more visible in Fig. 5, which shows the history of the height-averaged temperature of the heated wall

$$T_{\text{avg}} = \frac{1}{H}\int_0^H T_{\text{w}}(y)\,\mathrm{d}y. \tag{1}$$

Figure 5 shows also that the time of maximum temperatures decreases as the Rayleigh number increases.

Figure 6 shows the real-time evolution of the height-averaged thickness of the liquid region

$$s_{\text{av}} = \frac{1}{H}\int_0^H s(y)\,\mathrm{d}y. \tag{2}$$

This quantity is analogous (proportional) to the melt fraction reported in previous studies. The figure shows that s_{av} increases linearly in time: this behavior is to be expected in a melting experiment that is conducted at a constant heating rate. A useful function of Fig. 6 was that it allowed us to estimate in an 'aggregate' sense the value of the start-up time t_0. The time t_0 was obtained by fitting a straight line to the first five points of each set of data and then intersecting this line with the abscissa. By subtracting t_0 from the real time t, we were able to project all the melting curves on the dimensionless plane of Fig. 7, where the abscissa parameter is now the corrected time

$$\theta_*^{(0)} = Ste_* \frac{\alpha}{H^2}(t - t_0). \tag{3}$$

Therefore, the dimensionless $\theta_*^{(0)}$ values used in correlating the experimental results (Figs. 7 and 8) rep-

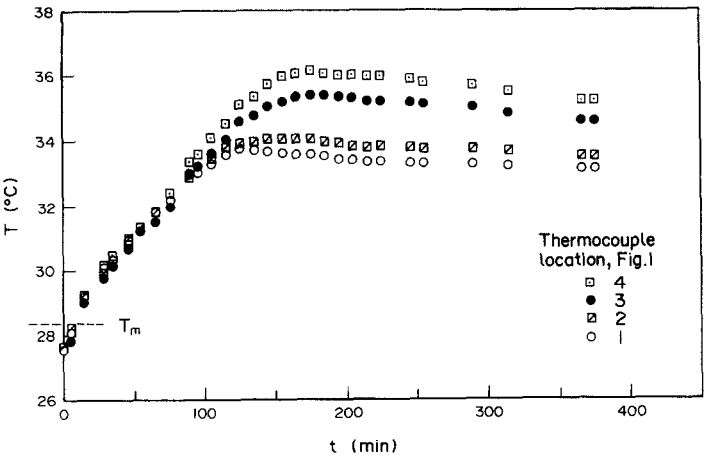

FIG. 4. The history of the temperature distribution along the heated plate ($Ra_* = 7.13 \times 10^{12}$).

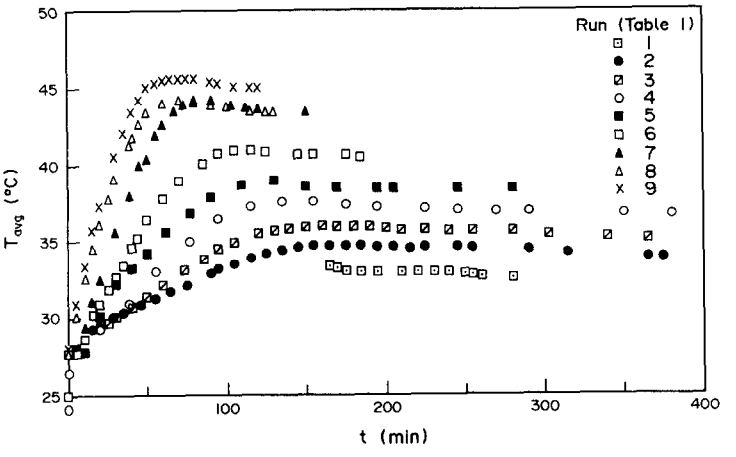

FIG. 5. The history of the height-averaged temperature of the heated plate.

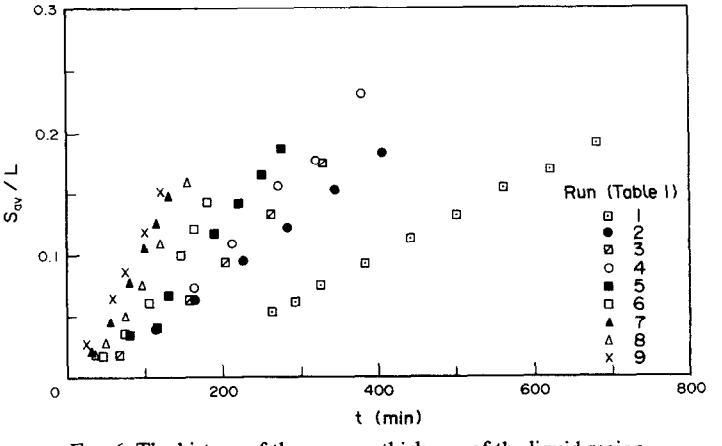

FIG. 6. The history of the average thickness of the liquid region.

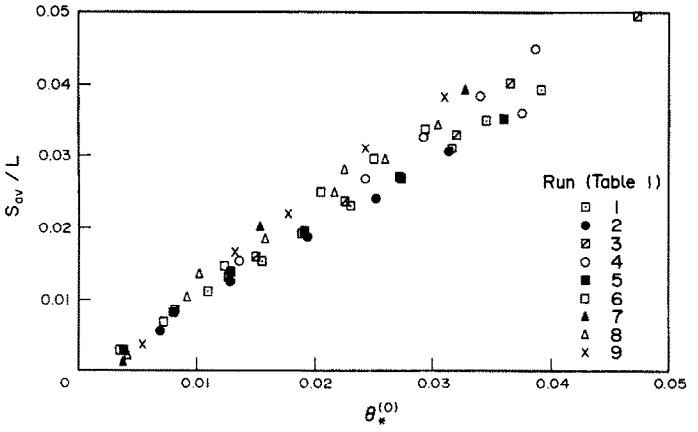

FIG. 7. Dimensionless representation of the melt fraction measurements reported in Fig. 6.

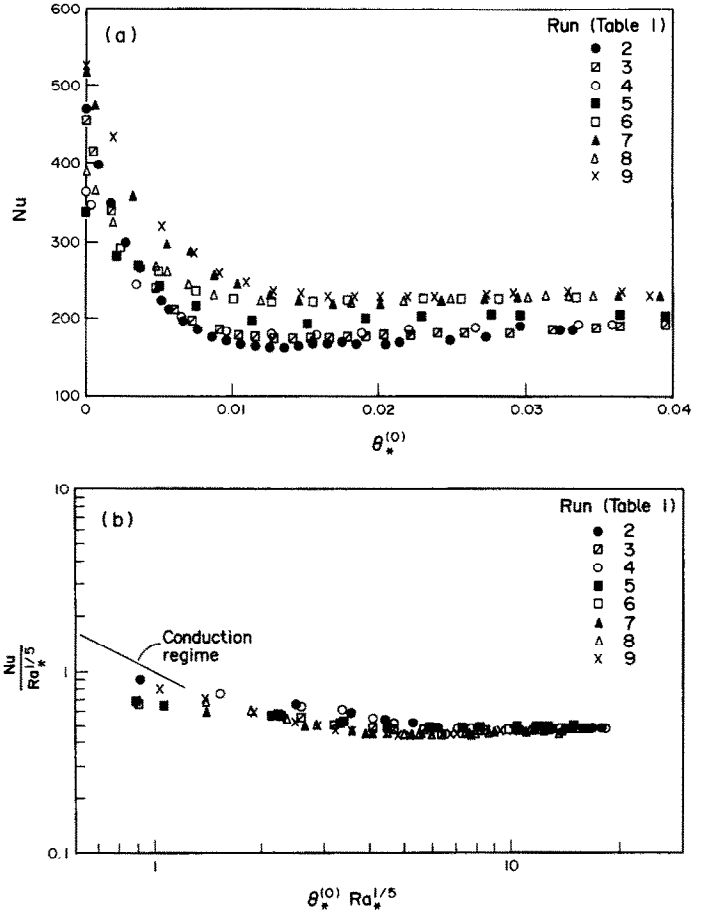

FIG. 8. Nusselt number curves corresponding to the average temperature measurements of Fig. 5.

resent the dimensionless time counted after the end of the start-up interval. In equation (3), α and H are the liquid thermal diffusivity and the height of the two-phase interface. The dimensionless group Ste_* is the Stefan number based on the constant heating rate

$$Ste_* = \frac{c(q''H/k)}{h_{sf}} \tag{4}$$

where c, k and h_{sf} are the liquid specific heat, thermal conductivity and latent heat of melting.

The data displayed in Figs. 5–8 were generated by the nine experimental runs summarized in Table 1. The Rayleigh number (Ra_*) and the heating rate Stefan number (Ste_*) increase from one run to the next. The Rayleigh number Ra_* is time independent, because it is based on the imposed heat flux q''

Table 1. Summary of the experimental runs described in Figs. 2–8 and 13

Run	Ra_*	Ste_*	Ste_s
1	4.9×10^{12}	0.019	0.017
2	7.1×10^{12}	0.026	0.014
3	9.0×10^{12}	0.031	0.013
4	1.1×10^{13}	0.037	0.016
5	1.4×10^{13}	0.045	0.046
6	1.9×10^{13}	0.056	0.032
7	2.3×10^{13}	0.067	0.032
8	2.3×10^{13}	0.067	0.018
9	2.6×10^{13}	0.074	0.017

$$Ra_* = \frac{g\beta H^4 q''}{\alpha\nu k} \tag{5}$$

where g, β and ν are the gravitational acceleration, volume expansivity of the liquid, and kinematic viscosity.

The solid phase Stefan number is defined by

$$Ste_s = \frac{c_s(T_m - T_s)}{h_{sf}} \tag{6}$$

where c_s is the specific heat of the solid, and T_s the uniform initial temperature of the entire enclosure. In these experiments we aimed for the limit $Ste_s \to 0$, by heating and/or cooling the initial solid such that T_s approached the melting point T_m. The small departures from zero that are exhibited by the Ste_s values in Table 1 are due to the fact that the laboratory temperature changed, that is, from summer to winter.

Runs 7 and 8, for example, differ only with respect to solid phase Stefan number. These two runs produced the second and third highest curves in Fig. 5. The curves show that changes in Ste_s affect primarily the slope of the rising portion of the $T_{avg}(t)$ curve, i.e. the pure conduction regime of the melting process. As the degree of solid subcooling (Ste_s) increases, the rate of temperature increase experienced by the heated wall decreases. The two curves approach the same plateau in the convection regime, indicating that the transient conduction phenomenon in the solid (triggered when Ste_s is finite) has already run its course.

Figure 8(a) shows the Nusselt number vs dimensionless time curves that correspond to the average wall temperature measurements of Fig. 5. The Nusselt number is this time based on the average temperature difference $(T_{avg} - T_m)$

$$Nu = \frac{q''H}{k(T_{avg} - T_m)} \tag{7}$$

where T_m is the temperature of the solid–liquid interface (the melting point). The shape of each Nu curve resembles the 'van der Waals curve' shape revealed by heat transfer measurements in experiments in which the heating was provided by a constant temperature wall (e.g. Webb and Viskanta [7]). In Fig. 8, however, the minimum in the Nu curve is considerably less pronounced than in isothermal-wall experiments. In fact, the minimum practically disappears as Ra_* increases.

The analysis presented in Section 3 suggests that the Nu data of Fig. 8(a) can be correlated by a unique relation between $Nu/Ra_*^{1/5}$ and $\theta_* Ra_*^{1/5}$. Subjecting the data of Fig. 8(a) to this transformation we obtain Fig. 8(b). This correlation works very well in the convection-dominated end of the process, where the data fall on the horizontal line

$$\frac{Nu}{Ra_*^{1/5}} \cong 0.491. \tag{8}$$

The standard deviation of the Nu data with respect to this asymptote is only 1.8%.

In the conduction-dominated extreme the data diverge somewhat, and their approach to the theoretical conduction limit (the solid line, $Nu = \theta_*^{-1}$) is not nearly as smooth. The chief reason for this behavior is the uncertainty associated with the values of $\theta_*^{(0)}$ in the small-time limit of each run (recall the approximate character of the start-up time calculation). Two additional reasons are the disappearance of the Nu minimum as Ra_* increases, and the effect of solid subcooling (Ste_s). We saw already in the discussion of Fig. 5 that the Ste_s effect is noticeable precisely in the conduction-dominated regime, even though the actual Ste_s values are much smaller than one (Table 1).

3. ANALYSIS OF THE CONVECTION REGIME

In this second part of the study, we report an analytical solution for the flow and heat transfer processes when the heated wall and the two-phase interface are lined by distinct boundary layers (i.e. in the 'convection regime'). In the present analysis we consider only the early part of this regime in order to be able to assume that the two-phase interface is sufficiently straight and vertical. In other words, the regime that is analyzed below occurs before the 'late' convection stages illustrated by the photographs of Fig. 2.

The analysis consists of developing boundary layer solutions for the flows near the heated wall and the two-phase interface, and then matching these two solutions to a unique solution for the core region. This method is essentially the same as Gill's [8]. The novel features of the present problem are:

(i) asymmetric heating, because the two-phase interface is isothermal (T_m) and the solid side wall is subjected to uniform heat flux (q'');

(ii) relative movement between the two boundary layers, because the cold boundary layer moves away from the heated wall as the two-phase interface advances into the solid.

The second feature is the result of conducting the analysis of the cold boundary layer in a frame that is attached to the two-phase interface. In this way, *the motion of the interface is taken into account* and,

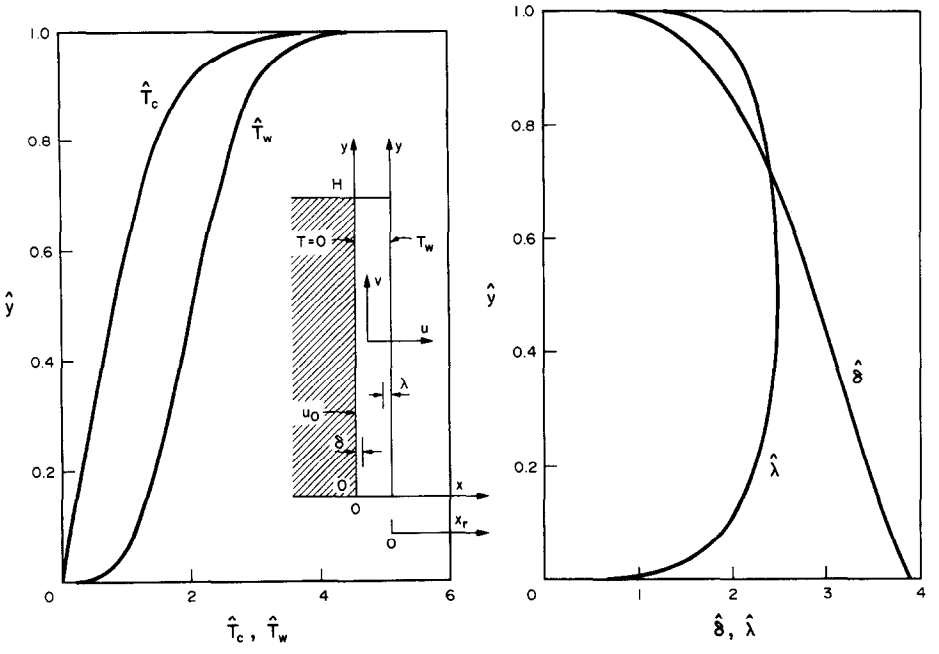

FIG. 9. Results of the boundary layer analysis in the limit of zero liquid superheat, $Ste = 0$.

through it, the effect of liquid superheating is documented by the solution.

3.1. *The cold boundary layer*

With reference to the x–y system of coordinates attached to the solid–liquid interface and shown in the detailed drawing inserted in Fig. 9, we recognize the boundary layer equations for momentum and energy conservation

$$\frac{\partial^3 v}{\partial x^3} + \frac{g\beta}{\nu}\frac{\partial T}{\partial x} = 0 \tag{9}$$

$$u\frac{\partial T}{\partial x} + v\frac{\partial T}{\partial y} = \alpha\frac{\partial^2 T}{\partial x^2}. \tag{10}$$

Worth noting is that the inertia terms have been neglected in writing the momentum equation: consequently, equation (9) is valid only inside the thermal boundary layer region (δ) in liquids the Prandtl numbers of which are greater than 1 (e.g. the liquid n-octadecane of the preceding experiments, the Prandtl number of which is 52).

Integral solutions for the temperature and flow distributions inside the cold boundary layer can be developed by assuming reasonable profiles for T and v, for example (Squire [9])

$$T = T_c\frac{x}{\delta}\left(2-\frac{x}{\delta}\right), \quad v = V\frac{x}{\delta}\left(1-\frac{x}{\delta}\right)^2. \tag{11}$$

In these expressions, T_c, V and δ are all functions of altitude (y). The function $T_c(y)$ represents the temperature distribution in the liquid core region, that is, in the liquid positioned beyond the outer edge of the boundary layer. All the temperatures used in this analysis (T, T_c, T_w) represent temperature differences measured above the melting point of the phase-change material. The temperature distribution along the two-phase interface is therefore $T = 0$.

The integral analysis based on equations (9)–(11) is straightforward, therefore, in the interest of brevity, its details will not be shown. The analysis consists of first integrating equation (9) from $x = 0$ to δ in order to evaluate the function $V(y)$. The next step is the integration of the energy equation (10), which marks the appearance of two additional unknowns, the melting velocity (u_0), with which the freshly formed liquid appears to be pushed into the cold boundary layer, and the entrainment velocity (u_δ) found at the outer edge. The same two unknowns emerge after integrating the mass conservation equation $\partial u/\partial x + \partial v/\partial y = 0$ across the boundary layer.

The entrainment velocity u_δ is then eliminated between the integral energy and mass conservation equations. The wall 'blowing' velocity u_0, on the other hand, is proportional to the liquid-side heat flux that arrives at the interface

$$u_0 = \frac{k}{\rho h_{sf}}\left(\frac{\partial T}{\partial x}\right)_{x=0}. \tag{12}$$

This particularly simple form of the energy continuity condition at the interface is due to: (a) the modelling of the solid as isothermal and at the melting point, (b) the fact that the system x–y is attached to the interface, and (c) the assumption that the interface is nearly plane (see p. 857 in Viskanta [2]).

After eliminating V, u_δ and u_0 in the manner described above, the analysis of the cold boundary layer yields a single equation for $\hat{\delta}$ and $\hat{T}_c$

$$2Ste\frac{\hat{T}_c^2}{\hat{\delta}}+\frac{\hat{T}_c}{36}\frac{d}{d\hat{y}}(\hat{T}_c\hat{\delta}^3)-\frac{1}{60}\frac{d}{d\hat{y}}(\hat{T}_c^2\hat{\delta}^3)=-2\frac{\hat{T}_c}{\hat{\delta}} \quad (13)$$

in terms of the dimensionless variables

$$\hat{y}=\frac{y}{H},\quad \hat{\delta}=\frac{\delta}{H}Ra_*^{1/5},\quad \hat{T}_c=\frac{T_c}{q''H/k}Ra_*^{1/5}. \quad (14)$$

These variables have been defined by noting that the proper scale of the temperature difference across the liquid space is $(q''H/k)Ra_*^{-1/5}$. The new group Ste is the Stefan number based on the proper temperature difference scale, and should not be confused with Ste_*

$$Ste=\frac{cq''H}{h_{sf}k}Ra_*^{-1/5}=Ste_*\,Ra_*^{-1/5}. \quad (15)$$

3.2. *The warm boundary layer*

The analysis of the flow along the heated plate repeats the steps outlined in the preceding subsection. The momentum and energy equations are the same as equations (9) and (10), in which (x, v, T) are replaced now by (x_r, v_r, T_r). The coordinate system x_r–y is attached to the heated plate, i.e. it is stationary with respect to the solid phase.

The Squire polynomials [9] chosen for the temperature and vertical velocity profiles are

$$T_r=(T_w-T_c)\left(1+\frac{x_r}{\lambda}\right)^2+T_c \quad (16)$$

$$v_r=V_r\frac{x_r}{\lambda}\left(1+\frac{x_r}{\lambda}\right)^2. \quad (17)$$

In these expressions, $\lambda(y)$ and $T_w(y)$ are the thickness of the warm boundary layer and the excess temperature distribution along the heated wall. The final energy integral equation produced by the analysis of the warm boundary layer is

$$\frac{1}{90}\frac{d}{d\hat{y}}[(\hat{T}_w-\hat{T}_c)\hat{\lambda}^3]+\frac{1}{36}(\hat{T}_w-\hat{T}_c)\hat{\lambda}^3\frac{d\hat{T}_c}{d\hat{y}}=\frac{2}{\hat{\lambda}}(\hat{T}_w-\hat{T}_c) \quad (18)$$

in which the dimensionless thermal boundary layer thickness and wall temperature are

$$\hat{\lambda}=\frac{\lambda}{H}Ra_*^{1/5},\quad \hat{T}_w=\frac{T_w}{q''H/k}Ra_*^{1/5}. \quad (19)$$

An additional equation is the condition of uniform heat flux from the side

$$q''=k\left(\frac{\partial T_r}{\partial x_r}\right)_{x_r=0}=\text{constant} \quad (20)$$

which translates into

$$\hat{T}_w-\hat{T}_c=\frac{\hat{\lambda}}{2}. \quad (21)$$

At this stage, the problem consists of solving a system of three equations (namely equations (13), (18) and (21)), which contain four unknowns $(\hat{\delta}, \hat{T}_c, \hat{\lambda}, \hat{T}_w)$. In order to close the problem, we focus next on the core region, the job of which is to bridge the gap between the two integral boundary layer solutions developed until now.

3.3. *The core region*

An important intermediate result of the integral analysis omitted from the preceding subsection is the entrainment velocity at the edge of the warm layer $(x_r=-\lambda)$

$$(u_r)_{-\lambda}=-\frac{d}{dy}\int_0^{-\lambda}v_r\,dx_r. \quad (22)$$

This is obtained by integrating the warm-side mass conservation equation $\partial u_r/\partial x_r+\partial v_r/\partial y=0$ and noting that the heated wall is impermeable. The corresponding entrainment velocity integral obtained in the analysis of the cold side (i.e. above equation (12)) is

$$u_\delta=u_0-\frac{d}{dy}\int_0^\delta v\,dx. \quad (23)$$

However, since the cold-side analysis was conducted in a frame attached to the moving interface, the true core velocity relative to a stationary frame is $u_\delta-u_0$, not u_δ.

We conclude that the horizontal entrainment velocities of the two boundary layers represent the same horizontal core flow if $u_\delta-u_0=(u_r)_{-\lambda}$. In view of equations (22) and (23) and the dimensionless variables defined earlier, this conclusion means

$$\frac{d}{d\hat{y}}(\hat{T}_c\hat{\delta}^3)=\frac{d}{d\hat{y}}[(\hat{T}_w-\hat{T}_c)\hat{\lambda}^3] \quad (24)$$

or, after integrating once

$$\hat{T}_c\hat{\delta}^3=[\hat{T}_w-\hat{T}_c]\hat{\lambda}^3+C. \quad (25)$$

The value of the constant C follows from the argument that at the bottom of the core $(\hat{y}=0)$ the liquid has the lowest attainable temperature $(\hat{T}_c=0$, i.e. the same as the two-phase interface), while the warm boundary layer 'starts' from the bottom $(\hat{\lambda}=0)$. These conditions are met simultaneously only if $C=0$. The same result is obtained by arguing that at the top of the enclosure $(\hat{y}=1)$, the core liquid reaches the highest temperature available, $\hat{T}_c(1)=\hat{T}_w(1)$, while the cold boundary layer starts from the top of the interface, $\hat{\delta}(1)=0$.

In conclusion, the core flow provides the horizontal portions of the circulation driven by the cold and warm boundary layers if

$$\hat{T}_c\hat{\delta}^3=(\hat{T}_w-\hat{T}_c)\hat{\lambda}^3. \quad (26)$$

The problem is now closed, because it consists of solving four equations, equations (13), (18), (21) and

(26), for a total of four functions of $\hat{y}$, namely, $\hat{\delta}$, $\hat{T}_c$, $\hat{\lambda}$ and $\hat{T}_w$.

3.4. *Results*

The above problem was solved numerically by introducing first the auxiliary variable $F = \hat{\delta}^3\hat{T}_c$, and then eliminating $\hat{T}_w$, $\hat{\delta}$ and $\hat{\lambda}$ between equations (13), (18), (21) and (26). What is left is a set of two first-order differential equations in $\hat{T}_c$ and F, the boundary conditions for which are $\hat{T}_c = F = 0$ at $\hat{y} = 0$, and $F = 0$ at $\hat{y} = 1$.

The two-equation system described above was solved using a shooting method in which the integration proceeds from $\hat{y} = 0$ to 1. The object of this method was to achieve the correct end-condition $F(1) = 0$, by properly adjusting the starting guess that had to be made for the value of $\hat{T}_c/F$. The integration was performed using the fourth-order Runge–Kutta method, the error of which was of the order of $(\Delta\hat{y})^5$, where $\Delta\hat{y}$ is the size of the step in the march from $\hat{y} = 0$ to 1. Double precision was employed in all the calculations. The shooting error—defined as the difference between the calculated $F(1)$ value and the desired one (zero)—was less than 10^{-9}.

A set of accurate $\hat{T}_c(\hat{y})$ and $F(\hat{y})$ functions was obtained in this manner for each assumed value of *Ste*. From these, it was easy to deduce the remaining parts of the solution, namely, $\hat{T}_w$, $\hat{\delta}$ and $\hat{\lambda}$. The final results are illustrated in Figs. 9–12. Table 2 uses the values of the core temperature distribution at zero liquid superheat, to show that the step size that was used in our calculations ($\Delta\hat{y} = 5 \times 10^{-4}$) is sufficiently small.

Figure 9 shows the complete solution for the case of zero liquid superheat. The core and heated wall temperatures increase monotonically with altitude, while $\hat{T}_w$ is always greater than $\hat{T}_c$. Furthermore, the temperature difference $\hat{T}_w - \hat{T}_c$ is nearly constant along the central portion of the height H. The values of both $\hat{T}_c$ and $\hat{T}_w$ are finite at the top of the enclosure.

Table 2. The effect of integration step size on the core temperature $\hat{T}_c(\hat{y})$ when $Ste = 0$

$\Delta\hat{y}$	$\hat{T}_c(0.1)$	$\hat{T}_c(0.5)$	$\hat{T}_c(0.9)$
5×10^{-4}	0.153835	0.795721	1.956636
10^{-4}	0.153824	0.795638	1.955803
2.5×10^{-5}	0.153825	0.795643	1.956060
10^{-5}	0.153832	0.795620	1.955961

The right-hand side of Fig. 9 shows that the thickness of the warm boundary layer ($\hat{\lambda}$) is nearly constant over most of the surface of the heated wall. This finding is in agreement with a feature described earlier by an analysis of pure natural convection in an enclosure heated and cooled with uniform heat flux from the side [6]. The thickness of the cold boundary layer that descends along the interface ($\hat{\delta}$) increases monotonically in the downward direction. This feature agrees with Gill's [8] description of boundary layer convection in an enclosure with differentially heated isothermal side walls.

Figure 10 shows the changes in $\hat{T}_c(\hat{y})$ and $\hat{T}_w(\hat{y})$ as the Stefan number increases. The core temperature decreases substantially, that is, it approaches the temperature of the two-phase interface ($\hat{T} = 0$). The temperature of the heated wall decreases also, but in a considerably less noticeable way. In conclusion, the effect of increasing the liquid thermal inertia (*Ste*) is

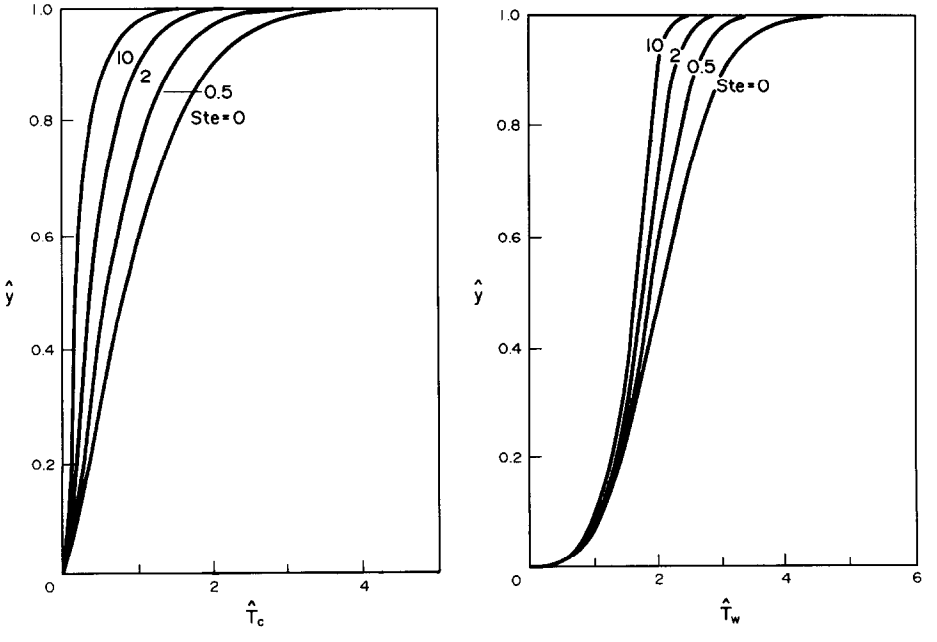

FIG. 10. The *Ste* effect on the core and wall temperature distributions.

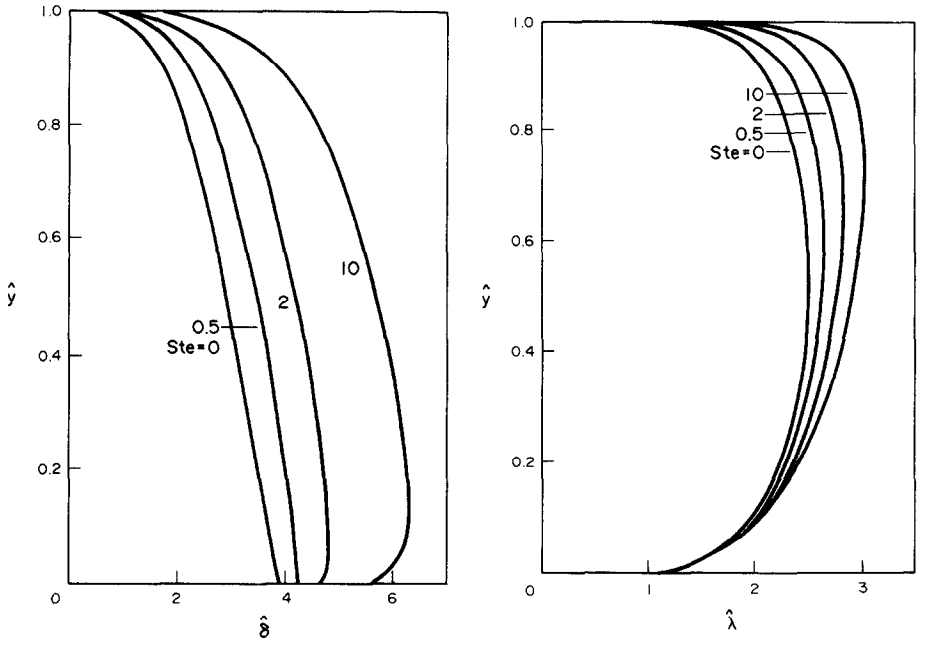

FIG. 11. The *Ste* effect on the thickness of the two boundary layers.

to depress the temperature distribution throughout the liquid region.

Figure 11 shows that both boundary layer thicknesses increase as the Stefan number increases, the more sensitive of the two being $\hat{\delta}$. In addition to the change in the size of $\hat{\delta}$, we see a change in its shape: when *Ste* is greater than approximately 0.5, the function $\hat{\delta}(\hat{y})$ is no longer monotonic.

Finally, Fig. 12 shows the effect of liquid superheat on the integral $\Phi(Ste)$

$$\Phi(Ste) = \int_0^1 2\frac{\hat{T}_c}{\hat{\delta}}\,d\hat{y} \tag{27}$$

which appears in the calculation of the total instantaneous melting rate, equation (12)

$$\int_0^H u_0\,dy = \frac{q''H}{\rho h_{sf}}\Phi(Ste). \tag{28}$$

In the limit of negligible liquid thermal inertia ($Ste = 0$), the entire heat input ($q''H$) is devoted to melting, therefore $\Phi(0) = 1$. The liquid-superheat factor Φ decreases noticeably as *Ste* increases, indicating that the total melting rate decreases when a fraction of the total heat input must overcome the thermal inertia of the freshly created liquid.

4. DISCUSSION

In this two-part study we have combined experiments with theory in order to describe the main

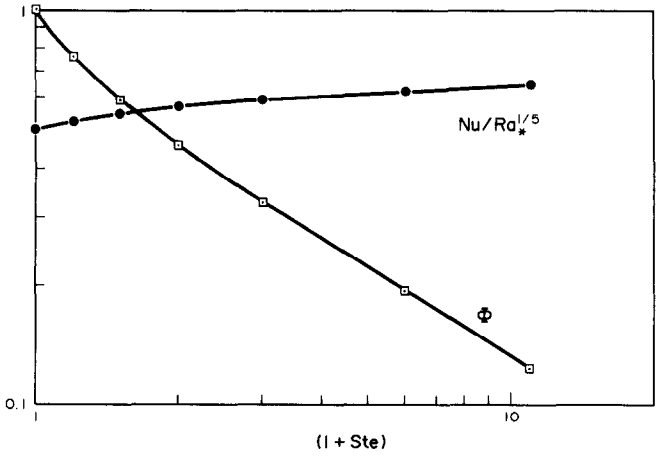

FIG. 12. The *Ste* effect on the total melting rate (Φ) and the overall Nusselt number for heating through the side wall.

characteristics of the phenomenon of melting in an enclosure heated at a constant rate. We relied on experimental observations of the evolution of the two-phase interface in order to construct the boundary-layer analysis presented in Section 3. This analysis invites another look at the experimental measurements obtained in the convection regime.

The curve labeled $Nu/Ra_*^{1/5}$ in Fig. 12 shows the manner in which the Nusselt number is expected to vary with the degree of liquid superheating. This curve was obtained from the theoretical solution described in the preceding section. Recalling the Nu definition (7), it is easy to prove that

$$\frac{Nu}{Ra_*^{1/5}} = \left(\int_0^1 \hat{T}_w \, d\hat{y} \right)^{-1} \tag{29}$$

i.e. that the warm-side Nusselt number is proportional to the inverse of the height-averaged value of the wall temperature. The ratio $Nu/Ra_*^{1/5}$ increases weakly as Ste increases. In the $Ste \to 0$ limit, which represents the domain of the experiments described in Section 2, the theoretical ratio $Nu/Ra_*^{1/5}$ approaches 0.4974. This result agrees very well (within 5%) with the empirical correlation for the convection-dominated limit, equation (8). Since many of the experimental data were obtained in late stages of the convection regime, such a high level agreement suggests that the nearly-straight-interface assumption (assumption (c) under equation (12)) is not critical when it comes to predicting the overall Nusselt number analytically.

Another feature anticipated by the boundary layer analysis of Section 3 is the temperature gradient along the heated wall. Figure 13 shows the measured temperature gradients in the convection regimes of each of the nine experimental runs (Table 1). In the convection regime, the temperature distribution between probes 1–4 (Fig. 1) was practically linear. Figure 13 shows also the theoretical value that can be read off the $Ste = 0$ curve on the right-hand side of Fig. 10. The theoretical line falls above the experimental measurements: this relative position can be attributed to the vertical conduction through the aluminum plate of the heated wall (Fig. 1), the tendency of which is to make the wall temperature distribution more uniform.

The analysis of Section 3 suggests that in the convection regime the dimensionless wall temperature gradient $d\hat{T}_w/d\hat{y}$ should be insensitive to changes in the Rayleigh number. This feature is confirmed by all the measurements. The important contribution of the theory of Section 3 is that it predicts correctly the manner in which the wall temperature gradient varies with the properties and dimensions of the system. In addition, the *average* wall temperature revealed by experiments agrees very well with the theory (see the right-hand side of equation (29), and the discussion below it).

Finally, the Nusselt number correlation developed in this study for the convection regime, equations (8) and (29), can be compared with the published correlations for the 'quasi-steady' regime in an enclosure heated through an isothermal wall. Raising both sides of equation (8) to the power 5/4 we obtain

$$Nu \cong 0.411 \left[\frac{g\beta H^3 (T_{avg} - T_m)}{\alpha \nu} \right]^{1/4} \tag{30}$$

in which the group in square brackets defines the more common Rayleigh number based on the average temperature difference, $Ra_{\Delta T}$. Equation (30) is comparable in form with the quasi-steady regime correlations for isothermal wall heating, e.g. the Bénard *et al.* correlation [10]

$$Nu \cong 0.33 Ra_{\Delta T}^{1/4} \tag{31}$$

and the Okada correlation [11]

$$Nu \cong 0.234 Ra_{\Delta T}^{0.266}. \tag{32}$$

In conclusion, the constant heating rate Nu results (30) are higher than the corresponding Nu values

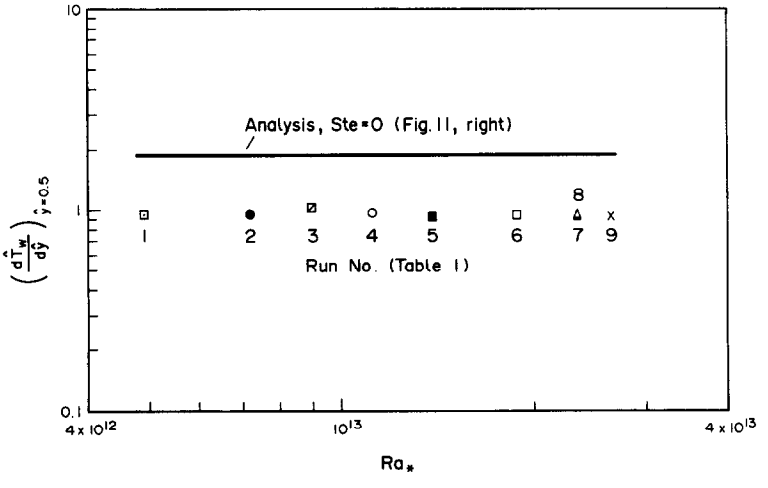

FIG. 13. The measured wall temperature gradient in the convection regime, vs the theoretical value corresponding to $Ste = 0$ (Fig. 10, right).

achieved with isothermal-wall heating. This situation is due to the different heating boundary condition used in the present experiments, and to the high Rayleigh number range (Table 1). Note that even in terms of $Ra_{\Delta T}$ (as opposed to Ra_*), the present Rayleigh number is considerably higher than the range covered previously. Using the identity $Ra_* = Ra_{\Delta T}\, Nu$, it is easy to show that the Ra_* range $4.9 \times 10^{12} - 2.6 \times 10^{13}$ of the present experiments corresponds to the $Ra_{\Delta T}$ range $2.9 \times 10^{10} - 1.1 \times 10^{11}$. Substituting $Ra_{\Delta T} = 10^{11}$ as a representative value in equations (30)–(32), we find that the present Nu result (equation (30)) is 19.7% larger than Bénard *et al.*'s equation (31), and 14.6% larger than Okada's equation (32).

The theoretical method of Section 3 was applied earlier to the study of natural convection-assisted melting [12], and melting in the presence of a porous matrix [13] near a vertical *isothermal* wall.

Acknowledgement—This work was supported by the Electric Power Research Institute through contract No. RP 8006-4, under the management of Dr Jong H. Kim.

REFERENCES

1. R. Viskanta, Phase-change heat transfer. In *Solar Heat Storage: Latent Heat Materials* (Edited by G. A. Lane). CRC Press, Boca Raton, Florida (1983).
2. R. Viskanta, Natural convection melting and solidification. In *Natural Convection: Fundamentals and Applications* (Edited by S. Kakac, W. Aung and R. Viskanta). Hemisphere, Washington, DC (1985).
3. W. D. Bennon and F. P. Incropera, Developing laminar mixed convection with solidification in a vertical channel, ASME Paper 87-HT-3, presented at the National Heat Transfer Conference, Pittsburgh, Pennsylvania, 9–12 August (1987).
4. D. Poulikakos and A. Bejan, Natural convection experiments in a triangular enclosure, *J. Heat Transfer* **105**, 652–655 (1983).
5. N. W. Hale and R. Viskanta, Photographic observation of the solid–liquid interface motion during melting of a solid heated from an isothermal vertical wall, *Lett. Heat Mass Transfer* **5**, 329–337 (1978).
6. S. Kimura and A. Bejan, The boundary layer natural convection regime in a rectangular cavity with uniform heat flux from the side, *J. Heat Transfer* **106**, 98–103 (1984).
7. B. W. Webb and R. Viskanta, On the characteristic length scale for correlating melting heat transfer data, *Int. Commun. Heat Mass Transfer* **12**, 637–646 (1985).
8. A. E. Gill, The boundary layer regime for convection in a rectangular cavity, *J. Fluid Mech.* **26**, 515–536 (1966).
9. H. B. Squire, Integral solution published in *Modern Developments in Fluid Dynamics* (Edited by S. Goldstein), Vol. 2, pp. 641–643. Dover, New York (1965).
10. C. Bénard, D. Gobin and F. Martinez, Melting in rectangular enclosures: experiments and numerical simulation, *J. Heat Transfer* **107**, 794–803 (1985).
11. M. Okada, Analysis of heat transfer during melting from a vertical wall, *Int. J. Heat Mass Transfer* **27**, 2057–2066 (1984).
12. A. Bejan, Analysis of melting by natural convection in an enclosure, *Int. J. Heat Fluid Flow* **10** (1989), to be published.
13. A. Bejan, Theory of melting with natural convection in an enclosed porous medium, *J. Heat Transfer* **111** (1989), to be published.

FUSION DANS UNE CAVITE CHAUFFEE A FLUX CONSTANT

Résumé—On décrit une étude en deux parties de la fusion, dépendante du temps, d'un matériau à changement de phase chauffé à flux constant par le côté d'une cavité. La première partie décrit des mesures expérimentales avec de l'octadécane dans une cavité de 74 cm. Les nombres de Rayleigh basés sur le flux sont de l'ordre de 10^{13} et les configurations du mouvement du fluide sont faiblement turbulentes. La seconde partie de l'étude décrit analytiquement l'effet de surchauffe du liquide, à l'aide d'une solution par raccordement de couche limite, pour le régime de convection des mécanismes de transfert de chaleur et de fusion. Les nombres de Nusselt calculés s'accordent très bien avec la formule empirique basée sur les expériences.

SCHMELZVORGANG IN EINEM EINSCHLUSS BEI KONSTANTEM HEIZWÄRMESTROM

Zusammenfassung—Die Abhandlung beschreibt eine zweiteilige Untersuchung des instationären Schmelzvorgangs in einem eingeschlossenen Phasenwechselmaterial durch einen konstanten Heizwärmestrom auf einer Seite. Der erste Teil beschreibt Messungen an n-Oktadekan in einem 74 cm hohen Hohlraum. Die mit der Wärmestromdichte gebildete Rayleigh-Zahl ist dabei von der Größenordnung 10^{13}, die Flüssigkeitsströmung ist leicht turbulent. Der zweite Teil beschreibt die Flüssigkeitsüberhitzung analytisch mit Hilfe einer Lösung für die Grenzschichten im Bereich des konvektiven Wärmeübergangs und des Schmelzvorgangs. Die berechnete Beziehung für die mittlere Nusselt-Zahl stimmt sehr gut mit der empirisch ermittelten Korrelation überein.

ПЛАВЛЕНИЕ В ЕМКОСТИ ПРИ ПОСТОЯННОЙ СКОРОСТИ НАГРЕВА

Аннотация—Исследуется временная зависимость плавления вещества в емкости при нагреве сбоку с постоянной интенсивностью. В первой части описываются экспериментальные измерения для н-октадекана, проведенные в емкости высотой 74 см. В данном эксперименте числа Рэлея по тепловому потоку составляли 10^{13}, а режим течения жидкости являлся слаботурбулентным. Во второй части исследования эффект перегрева жидкости описывается аналитически методом "сращиваемых пограничных слоев" для конвективного режима теплопереноса и процесса плавления. Рассчитанное соотношение для осредненного числа Нуссельта хорошо согласуется с эмпирической зависимостью, полученной экспериментально.